Ghoreyshi, Mehdi CTR GB USAF USAFA USAFA/DFAN

From: Lofthouse, Andrew J LtCol USAF USAFA USAFA/DFAN
Sent: Thursday, May 29, 2014 2:41 PM
To: Ghoreyshi, Mehdi GB CTR USAF USAFA USAFA/DFAN
Subject: PA release

TO	ACTION	NAME, GRADE, DATE
USAFA/DFAN	coord	Russell M Cummings HQ10 30 May 14
USAFA/DFER	approve	Solti, AD22, 2 Jun 14
USAFA/DFAN	action	

USAFA-DF-PA-354
USAFA-DF-PA-355
USAFA-DF-PA-356

ACTION OFFICER: Lt Col Lofthouse, USAFA/DFAN Phone: DSN 333-9526

Due: 20140531

SUBJECT: Clearance for Material for Public Release USAFA-DF-PA-

1. PURPOSE. To provide security and policy review on the documents at Tab 1-3 prior to release to the public.

2. BACKGROUND.

Authors: 1. Keith Bergeron, Jurgen Siedel, Mehdi Ghoreyshi, Adam Jirasek, Andrew Lofthouse, Russell Cummings

2. Mehdi Ghoreyshi, Jurgen Seidel, Keith Bergeron, Adam Jirasek, Andrew Lofthouse, Russell Cummings

3. Mehdi Ghoreyshi, Michael Young, Adam Jirasek, Andrew Lofthouse, Russell Cummings

Title: 1. Numerical Study of Ram Air Airfoils and Upper Surface Bleed-Air Control

2. Prediction of Aerodynamic Characteristics of a Ram-Air Parachute

3. Validation of Unsteady Aerodynamic Models of a Generic UCAV Configuration

Circle one: Abstract Tech Report Journal Article Speech ***Papers*** Presentation Poster

Thesis/Dissertation Book Other: _____

Check all that apply (For Communications Purposes):

[] CRADA (Cooperative Research and Development Agreement) exists

[] Photo/ Video Opportunities [] STEM-outreach Related [] New Invention/ Discovery/ Patent

Description: 3 papers describing recent research work in the High Performance Computing Research Center in conjunction with NATO Task Group AVT-201 and Army NATICK Soldier Center.

Release Information: AIAA SciTech 2015, 16-20 June, 2014, Atlanta, GA

Previous Clearance information: NONE

Recommended Distribution Statement: Distribution A, Approved for Public release, distribution unlimited.

3. DISCUSSION. N/A

4. RECOMMENDATION. Sign coord block above indicating document is suitable for public release. Suitability is based solely on

the document being unclassified, not jeopardizing DoD interests, and accurately portraying official party.

//SIGNED//

ANDREW J. LOFTHOUSE, Lt Col, USAF

Director, High Performance Computing Research Center

3 Tabs

Surface Bleed-Air Control

1. Numerical Study of Ram Air Airfoils and Upper

Ram-Air Parachute

2. Prediction of Aerodynamic Characteristics of a

Generic UCAV Configuration

3. Validation of Unsteady Aerodynamic Models of a

--

ANDREW J. LOFTHOUSE, Lt Col, USAF
Assistant Professor of Aeronautics
Director, Modeling & Simulation Research Center
US Air Force Academy
(719) 333-9526
Andrew.Lofthouse@usafa.edu

USAFA-DF-PA-356

Validation of Unsteady Aerodynamic Models of a Generic UCAV Configuration

Mehdi Ghoreyshi[1]*, Michael E. Young[2]†, Adam Jirásek[1]‡
Andrew J. Lofthouse[1]§, Russell M. Cummings[1]¶

[1] *High Performance Computing Research Center, U.S. Air Force Academy*
USAF Academy, Colorado 80840
[2] *Defence Science and Technology Organisation, Melbourne, Victoria, 3207, Australia*

This work is part of the NATO STO Task Group AVT-201 Special Sessions being organized by the AIAA Applied Aerodynamics Technical Committee. Reduced-Order Modeling techniques based on response functions are presented and validated for unsteady aerodynamic prediction of a generic UCAV with trailing edge flaps. A hybrid unstructured mesh was generated to move these control surfaces and simulate the flow fields around the vehicle with a sting geometry available in the experiments. The Reynolds-averaged NavierStokes predictions were validated by wind-tunnel static and dynamic case measurements. The flow topology over the configuration is described for a range of angles of attack and control surface deflections. Validation results also highlight the effects of gaps present in the overset mesh on the predictions. The response functions with respect to angle of attack, pitch rate, and flap deflections are directly calculated from step motion simulations in CFD and a grid motion approach. An aerodynamic model is then created from these functions and used to predict the vehicle aerodynamic responses obtained from pitching and plunging oscillations. The predictions are in good agreement with time-accurate simulations at low angles of attack, whereas for higher angles of attack, some discrepancies are seen. The results presented show that these discrepancies are not due to the sting geometry available in CFD models.

Nomenclature

a	acoustic speed, m/s
b	wing span, m
c	reference length, m
C_D	drag coefficient, $D/q_\infty S$
C_L	lift coefficient, $L/q_\infty S$
C_l	roll moment coefficient, $M_x/q_\infty Sb$
C_{lw}	roll moment coefficient in wind axes
C_m	pitch moment coefficient in body axes, $M_y/q_\infty Sc$
C_{mw}	pitch moment coefficient in wind axes
$C_{m\alpha}$	indicial pitch moment coefficient with angle of attack, 1/rad

*Senior Aerospace Engineer, AIAA Senior Member
†Senior Aerospace Engineer, AIAA Member
‡Research Fellow, AIAA Senior Member
§Director, AIAA Senior Member
¶Professor of Aeronautics, AIAA Associate Fellow

Distribution A. Approved for Public Release. Distribution unlimited.

$C_{m\delta_f}$	indicial pitch moment coefficient with flap deflection, 1/rad
C_{mq}	indicial pitch moment coefficient with normalized pitch rate, 1/rad
C_n	yaw moment coefficient, $M_z/q_\infty Sb$
C_{nw}	yaw moment coefficient in wind axes
C_Y	side-force coefficient, $Y/q_\infty S$
C_Z	z-force coefficient, $Z/q_\infty S$
$C_{Z\alpha}$	z-force coefficient with angle of attack, 1/rad
$C_{Z\delta_f}$	z-force coefficient with flap deflection, 1/rad
C_{Zq}	z-force coefficient with normalized pitch rate, 1/rad
D	drag force, N
d	frequency, Hz
L	lift force, N
M_x	roll moment in body axes, N-m
M_y	pitch moment in body axes, N-m
M_z	yaw moment in body axes, N-m
$\bar{q}$	pitch rate, rad/s
q	normalized pitch rate, $\bar{q}c/V$, 1/rad
q_∞	dynamic pressure, Pa
Re	Reynolds number, $\rho Vc/\mu$
S	reference area, m^2
s	normalized time, $2Vt/c$
t^*	non-dimensional time step, Vt/c
t	time, s
V	velocity, m/s
x, y, z	grid coordinates, m
Y	side force, N
Z	Z-axis force, N

Greek

α	angle of attack, rad
δ_{fi}	inner flap deflection, rad
δ_{fo}	outer flap deflection, rad
ω	circular frequency, rad/s
ρ	density, kg/m^3
μ	air viscosity

I. Introduction

This paper focuses on the recent aerodynamic modeling efforts of the NATO STO Task Group AVT-201. The main objectives for the Group are to investigate the effects of deflection of control surfaces on the aerodynamic characteristics and dynamic Stability & Control (S&C) and to build S&C data bases from experimental and simulations.[1] The configuration considered is based on the Stability And Control CONfiguration, SACCON UCAV which was designed and built as part of AVT-161.[2] An extensive series of experiments were carried out at the German-Dutch wind tunnel facility in Braunschweig (DNW-NWB) and 14′x22′ NASA LaRC to understand and analyze the aerodynamic performance of this vehicle. These data were then used to validate several computational fluid dynamics (CFD) solvers and overcome the computational challenges for predicting complex vortex flow topology over the configuration. The results of the AVT-161 Task Group have been presented at the AIAA conference in 2010 within experimental[3,4,5] and numerical sessions.[6,7,8] These results were published in a special section of the Journal of Aircraft as well.[9,10,11]

The current state-of-art in the use of CFD for aircraft design is the generation of data for S&C and flight simulation. This modeling approach can be used for early detection of unwanted effects regarding

stability and control behavior. Previous NATO STO Task Groups were mostly focused on the simulation and validation of flow fields around complex geometries rather than generating flight simulation data bases. The wind tunnel experiments of these Task Groups were therefore carried out with a clean geometry or with non deflected control surfaces. SACCON wind tunnel model, for example, has no control surfaces. The X-31 model has control surfaces but they were not deflected in wind tunnel experiments and had a sealed gap between control surfaces and wings.[12] Unfortunately, no flight simulation model can be created from these experimental data because aircraft cannot maneuver without control surface deflections. However, there were few studies to investigate the aerodynamic behavior of a maneuvering SACCON by CFD. Vallespin et al,[13] for example, implemented a pair of control surfaces for their SACCON CFD model. These surfaces covered most of the wing sections span along the trailing edge. They used these surfaces to simulate several six degree-of-freedom(6-DOF) SACCON maneuvers in CFD. Ghoreyshi and Cummings[14] also defined a number of SACCON maneuvers and replayed them in CFD to investigate the unsteady aerodynamic behavior of the vehicle, although no control surface deflection was modeled. While these studies provide a great deal of insight into the vehicle's aerodynamic modeling, the accuracy and sensitivity of models cannot be assessed without having any experimental data. In this regard, the work of AVT-201 will focus on the development of S&C aerodynamic models from both CFD and experimental data. This will help to learn the impacts of experimental and CFD predictions on the flight simulation accuracy.

To reach the Task Group objectives, the SACCON model was modified to include conventional trailing edge devices for pitch, roll and yaw controls. Several different devices were initially designed and tested in the DNW-NWB wind tunnel; the geometry used in this work is known as DLR-F19 which has inboard and outboard control surfaces on the trailing edge of each wing and two control devices at the wing tips. In the present work only trailing edge control surfaces are considered. These surfaces have a hingeline located at 75%c, where c is the wing chord. The resulting model mounted (with a belly mounted support) on the Model Positioning Mechanism (MPM) system of the DNW-NWB wind tunnel facility. This setup allows forced sinusoidal oscillations in modes of pitch and yaw. The position of the belly sting connection is chosen to minimize the influence of the sting on the overall flow topology.[9] However, an offset can be seen in the experimental pitch moment due to the wake formed behind the belly mounted sting.[15] The sting geometry is therefore included in the CFD models of this work.

Static tests of the DLR-F19 wind tunnel model were conducted over an angle of attack range from about 0^o to 30^o and an sideslip angle range from about -10^o to 10^o with a number of control surface combinations. Dynamic tests were performed with pitch and yaw oscillations with no and minimum-maximum deflections of control surfaces. Note that in each test, control surfaces do not move relative to the wing. An aerodynamic database can be generated from these experimental data to study the vehicle's S&C, but a number of problems need to be addressed to use such a model: first, this database is only valid within the range of input data used for the model generation. For example, the experiments only covered 0^o, -20^o and 20^o control surface deflections. An interpolation/extrapolation approach can be used for extending the valid range to other flight conditions, however, these estimations might not be accurate and reliable. The second problem is based on the model limitation to predict unsteady aerodynamics. The DLR-F19 wind tunnel tests cannot model the dynamic behavior of control surfaces. Ghoreyshi and Cummings[16] showed that unsteady effects due to fast control surface deflections significantly change the amplitude and phase lags of predicted airloads compared with static (or steady-state) predictions.

With respect to the first problem, wind tunnel tests can be used to validate a CFD model; the model will then predict aerodynamic data for conditions not tested in the wind tunnel. Some of the papers in the NATO STO Task Group AVT-201 Special Sessions present the CFD validation results of the DLR-F19 wind tunnel models with and without control surfaces.[17,18,19,20,21] A problem of using CFD to fill tables is the mesh generation and the computational cost: to build an aerodynamic model using CFD, a separate high quality grid needs to be generated around aircraft for each control surface deflection. An aerodynamic model for stability and control also requires a large number of coupled computations for different values of motion frequency and amplitude for each configuration which makes time-accurate CFD simulations a very expensive approach. In this work, an overset grid approach is used to avoid the mesh regeneration problem. The overset grid, however, has gaps between the inboard and outboard edges of the control surfaces, while these gaps are sealed in the experiments. The control surfaces in the overset grid are also modified to have a semi-circular leading edge with a 2mm gap between surfaces and the wing. To investigate the effects of these gaps and geometry modifications on the CFD prediction, the results of overset grid are compared with predictions of two single grids with zero and maximum-minimum control surface deflections.

To include unsteady effects and make timely progress in the use of CFD for S&C, efforts over the last few years have been spent mainly on the development of a Reduced Order Model (ROM) using CFD from an appropriate training maneuver(s) and an accurate System IDentification (SID) approach.[22,23] The objective of the ROMs is to develop a model that significantly reduces the CFD simulation time required to create a full aerodynamics database, making it possible to accurately model aircraft static and dynamic characteristics (within the range of data used for model generation) from a number of time-accurate CFD simulations. These models need an initial or upfront cost to estimate, or identify, the unknown parameters. Once the model has been created, however, the aerodynamics prediction of a wide range of maneuvers can be determined in order of a few seconds. This work aims to assess the accuracy of predictions of a ROM based on indicial response method of Tobak.[24]

The transient aerodynamic response due to a unit step change in a forcing parameter, such as angle of attack or pitch rate or control surface deflection is a so-called "indicial function". Assuming that the indicial functions are known, the linear aerodynamic forces and moments induced in any maneuver can be estimated using the well-known Duhamel's superposition integral.[25] Tobak[24,26] formulated a nonlinear indicial response model for predicting aerodynamic responses to an arbitrary angle of attack variation as well. These models have then been used as a fundamental approach to represent the unsteady aerodynamic loads, in particular for two-dimensional airfoils. For wings and aircraft configurations, Ghoreyshi et al.[27] described an approach based on a grid motion technique for CFD-type calculation of linear and nonlinear response functions. Ghoreyshi and Cummings[28] later used this approach to generate indicial functions due to longitudinal and lateral forcing parameters of the SACCON UCAV and used these functions for predicting the unsteady aerodynamic responses to aircraft six degrees of freedom maneuvers.

The present study develops ROMs based on the linear and nonlinear indicial response methods for computing the aerodynamic loads of the DLR-F19 with and without control surfaces. The response functions with respect to angle of attack, pitch rate, and control surface deflections are directly calculated using unsteady RANS simulations with a grid motion technique. The models will then be evaluated for several pitching and plunging motions at different amplitudes and frequencies which were replayed directly through an unsteady CFD simulation.

II. Formulation

A. CFD Solver

Cobalt solves the unsteady, three-dimensional, compressible Navier-Stokes equations in an inertial reference frame. Arbitrary cell types in two or three dimensions may be used; a single grid therefore can be composed of different cell types.[29] In Cobalt, the Navier-Stokes equations are discretized on arbitrary grid topologies using a cell-centered finite volume method. Second-order accuracy in space is achieved using the exact Riemann solver of Gottlieb and Groth,[30] and least squares gradient calculations using QR factorization. To accelerate the solution of the discretized system, a point-implicit method using analytic first-order inviscid and viscous Jacobians is used. A Newtonian sub-iteration method is used to improve the time accuracy of the point-implicit method. Tomaro et al.[31] converted the code from explicit to implicit, enabling Courant-Friedrichs-Lewy (CFL) numbers as high as 10^6. In Cobalt, the computational grid can be divided into group of cells, or zones, for parallel processing, where high performance and scalability can be achieved even on ten thousands of processors.[32]

B. Turbulence Modeling

Some available turbulence models in Cobalt are the Spalart-Allmaras (SA) model, Spalart-Allmaras with Rotation Correction (SARC), and Delayed Detached-eddy simulation (DDES) with SARC. The SA model[33] is the most popular one-equation model that solves a transport equation for a modified eddy-viscosity coefficient. The SA model can be written in general form as[34]

$$\frac{D\tilde{\nu}}{Dt} = P + D_{diff} + D_{diss} \tag{1}$$

where $\tilde{\nu}$ is related to the kinematic eddy viscosity, P is the turbulence due to production, D_{diff} is the turbulence due to gradient of diffusion, and D_{diss} is the near wall dissipation of turbulent kinematic viscosity.

The production term is given by

$$P = C_{b1}(1 - f_{t2})W\tilde{\nu} \tag{2}$$

where W is the magnitude of vorticity. The SA model has been calibrated using a wide range of experimental data of several well-documented flow cases and has proven to be robust, relatively low cost, and simple because it does not need standard wall functions provided that $y^+ \sim 1$ near the wall.[35] On the other hand, the model depends on the global minimum wall distance and cannot accurately predict the unsteady features of vortex breakdown and massively separated flows. It has been shown that eddy-viscosity-based models improve mean flow predictions if an empirical rotation and streamline curvature correction is incorporated.[36] Spalart and Shur[37] modified the original SA turbulence model with Rotation and Curvature correction. In the SARC model, the production term in the eddy viscosity transport equation is multiplied by the rotation function given by

$$P = C_{b1}(f_{r1} - f_{t2})W\tilde{\nu} \tag{3}$$

where f_{r1} is the rotation correction factor. The SARC model has been widely used for aerodynamic prediction of aircraft with vortical flows. However, the use of hybrid RANS/LES (large-eddy simulation) is still required for predicting unsteady separated flows. A hybrid RANS/LES approach is the Delayed Detached-eddy simulation (DDES) originally proposed by Spalart et al.[38] In this model, SA model is applied to the boundary layer region and LES is used for the separated regions. The approach is substantially less costly than LES, while it can achieve better accuracy than SA model for predicting separated flows.[39] DDES models have been use with other turbulence models as well. These models largely depend on the grid spacing and the prediction of the boundary layer.

C. Overset Grid Approach

Cobalt uses an overset grid method which allows the independent translation and rotation of each grid around a fixed or moving hinge line. In this method, overlapping grids are generated individually, without the need to force grid points aligned with neighboring components.[40] In Cobalt, the overlapping grids are treated as a single mesh using a grid-assembly process. This includes a hole-cutting procedure in overlapping regions and interpolation between overlapping grids. The translation and rotation of overset grids around the hinge line are input to the code using a Grid Control File (GCF). The hinge line is defined by a reference point and a vector combination. The rotations are based on the right-hand rule and consist of angles in an order of pitch, yaw, and roll angle. These angles are estimated from the deflection angle of a control surface and the relative angles between the hinge line and grid coordinate axes.

D. Indicial Response Theory

In this work only longitudinal forces and moments acting on the DLR-F19 are considered. It is assumed that unsteady effects on the drag force are small. In ROMs of this work, lift and pitch moment depend on the angle of attack, pitch rate, and deflection of flap surfaces. Indicial responses due to a unit step change in angle of attack, α, normalized pitch rate, q, the inboard and outboard flaps, δ_{fi} and δ_{fo}, are denoted by C_{j_α}, C_{j_q}, $C_{j_{\delta_{f_i}}}$ and $C_{j_{\delta_{f_o}}}$ respectively; where $C_j = [C_L, C_m]$ represent lift and pitch moment coefficients. The unsteady lift and pitch moment are then calculated by adding Duhamel's integrals with respect to all inputs, i.e.

$$\begin{aligned} C_j(t) =& C_{j_0} + \alpha(0)C_{j\alpha}(t) + \delta_{fi}(0)C_{j_{\delta_{f_i}}}(t) + \delta_{fo}(0)C_{j_{\delta_{f_o}}}(t) + \int_0^t C_{j\alpha}(t-\tau)\frac{d\alpha(\tau)}{d\tau}d\tau + \\ & \int_0^t C_{jq}(t-\tau)\frac{dq(\tau)}{d\tau}d\tau + \int_0^t C_{j_{\delta_{f_i}}}(t-\tau)\frac{d\delta_{fi}(\tau)}{d\tau}d\tau + \int_0^t C_{j_{\delta_{f_o}}}(t-\tau)\frac{d\delta_{fo}(\tau)}{d\tau}d\tau \end{aligned} \tag{4}$$

where C_{j_0} denote the zero-angle of attack lift and pitch moment coefficients and are found from static calculations; $\alpha(0)$, $\delta_{fi}(0)$ and $\delta_{fo}(0)$ are the angle of attack, inboard-flap and outboard-flap deflections at time zero or the initial time of motion. Note that these terms are different from C_{j_0}. The motions of this

work start from a steady-state solution with $q(0) = 0$ and therefore the term of $q(0)C_{jq}(t)$ was not added to the equation. Using "differential theorem of the convolution integral", equation 4 changes to:

$$\begin{aligned} C_j(t) =& C_{j_0} + \frac{d}{dt}\left[\int_0^t C_{j\alpha}(t-\tau)\alpha(\tau)d\tau\right] + \frac{d}{dt}\left[\int_0^t C_{jq}(t-\tau)q(\tau)d\tau\right] + \\ & \frac{d}{dt}\left[\int_0^t C_{j_{\delta_{fi}}}(t-\tau)\delta_{fi}(\tau)d\tau\right] + \frac{d}{dt}\left[\int_0^t C_{j_{\delta_{fo}}}(t-\tau)\delta_{fo}(\tau)d\tau\right] \end{aligned} \tag{5}$$

These equations predict lift and pitch moment responses in the linear regime of flow. Ghoreyshi and Cummings[28] extended this model to a nonlinear situation by calculating indicial functions at different angles of attack and Mach numbers and then used the model in predicting aerodynamic responses to different motions. In this study, a nonlinear model is considered where C_{j_α} response depends on the angle of attack only. Mach number variation is not considered because all motions were performed at a fixed Mach number that was used to generate ROMs. It is assumed that the response functions with respect to the pitch rate do not vary with the changes in angle of attack for the motions studied. This is a reasonable assumption for low to moderate angles of attack range based on aerodynamic prediction methods described in aircraft design textbooks.[41] The control surface motions are performed at a fixed angle of attack and Mach number, but control surface responses change with flap angles. This work's nonlinear model is therefore written as:

$$\begin{aligned} C_j(t) =& C_{j_0} + \frac{d}{dt}\left[\int_0^t C_{j\alpha}(t-\tau,\alpha)\alpha(\tau)d\tau\right] + \frac{d}{dt}\left[\int_0^t C_{jq}(t-\tau)q(\tau)d\tau\right] + \\ & \frac{d}{dt}\left[\int_0^t C_{j_{\delta_{fi}}}(t-\tau,\delta_{fi})\delta_{fi}(\tau)d\tau\right] + \frac{d}{dt}\left[\int_0^t C_{j_{\delta_{fo}}}(t-\tau,\delta_{fo})\delta_{fo}(\tau)d\tau\right] \end{aligned} \tag{6}$$

This model has been used to predict unsteady and nonlinear aerodynamic responses of the DLR-F19 pitching and plunging motions at different amplitudes and frequencies. The model also can predict unsteady airloads due to dynamic control surface deflections.

E. CFD Calculation of Response Functions

The step response is a mathematical concept which is very difficult, if not impossible, to be measured from experiment. Limited analytical expressions of indicial functions exist for two-dimensional airfoils.[42] However, these analytical expressions are not valid for aircraft configurations due to the three-dimensional tip vortices. CFD therefor offers a viable method to estimate 3D indicial functions but in the absence of credible wind tunnel test data, it is difficult to validate CFD predictions. For this reason, ROM predictions are typically validated against full-order simulations or available experimental data of different maneuvers.

Special considerations are required to simulate step responses in CFD. Singh and Baeder[43] used a surface transpiration approach to directly calculate the angle of attack indicial response using CFD. Ghoreyshi et al.[27] also described an approach based on a grid motion technique for CFD-type calculation of linear and nonlinear response functions. In this paper, the response functions due to angle of attack, pitch rate, and flap deflections are calculated using CFD and the grid motion approach.

Cobalt uses an arbitrary Lagrangian-Eulerian formulation and hence allows all translational and rotational degrees of freedom.[27] The code can simulate both free and specified six degree of freedom (6DoF) motions. The rigid motion is specified from a motion input file. For the rigid motion the location of a reference point on the aircraft is specified at each time step. In addition the rotation of the aircraft about this reference point is also defined using the rotation angles of yaw, pitch, and roll (bank). The aircraft reference point velocity, v_a, in an inertial frame is then calculated to achieve the required angles of attack and sideslip, and the forward speed. The velocity is then used to calculate the location. The initial aircraft velocity, v_0, is specified in terms of Mach number, angle of attack and side-slip angle in the main file. The instantaneous aircraft location for the motion file is then defined from the relative velocity vector, $v_a - v_0$.

The response function due to pitch rate, i.e. C_{jq} for $j = L, m$ are calculated only at zero degrees angle of attack and for the clean configuration. This value is next used to estimate the second integral in Eqs. 5 and 6 , however, the estimation of nonlinear $C_{j\alpha}(t, \alpha)$ for $j = L, m$ needs more explanation. Assume a set of angle of attack samples of $\alpha = [\alpha_1, \alpha_2, ..., \alpha_n]$, where the spacing can be uniform or non-uniform. The

response functions at each angle of $\alpha_k, k = 1, 2, ..., n$ degrees are calculated by holding the angle of attack fixed at $\alpha = \alpha_k$ degrees, and then performing a small step in the angle of attack to $\alpha = \alpha_k + \Delta\alpha$. The response functions are then computed by taking the differences between time-varying responses occurring after the step and the steady-state solution at $\alpha = \alpha_k$ degrees, and dividing them by the magnitude of the step.[26]

The calculation of inboard and outboard flap responses, i.e. $C_{j_{\delta_{fi}}}(t, \delta_{fi})$ and $C_{j_{\delta_{fo}}}(t, \delta_{fo})$, is very similar to the angle of attack response calculation method: again assuming a set of deflection angles of $\delta = [\delta_1, \delta_2, ..., \delta_n]$, the response functions at each flap angle of $\delta_k, k = 1, 2, ..., n$ degrees are calculated by performing a steady-state solution with holding $\delta = \delta_k$ degrees, and then performing a step in the deflection angle to $\delta = \delta_k + \Delta\delta$. The response functions are then computed by taking the differences between the time-varying responses occurring after the step and the steady-state solution at $\delta = \delta_k$ degrees, and dividing them by the magnitude of the step.

III. Test Case

The DLR-F19 configuration is shown in Figure 1 (a). This vehicle has a lambda wing planform, similar to the SACCON wing, and has a leading edge sweep angle of 53 deg as shown in Figure 1 (b). The root chord is approximately one meter and the wing span is 1.53 m. The main sections of the model are the fuselage, the wing section, the wing tip. The DLR-F19 UCAV has control surfaces located on the left and right hand side along the trailing edge of the outer wings and at the wing tips. The hinge lines of the trailing edge control surfaces are located at 75% of the outer wing cord. The configuration consists of three different profiles at the root section of the fuselage, including two sections with the same profile at the inner wing that form the transition from the fuselage to the wing and the outer wing section. The wings leading edge is parallel to its trailing edges as well. Finally, the outer wing section profile is twisted by five degrees around the leading edge to reduce the aerodynamic loads and to shift the onset of flow separation to higher angles of attack.

The DLR-F19 model has been tested in the DNW-NWB wind tunnel facility with different combinations of trailing edge control surface deflections. The deflections covered in the experiments were -20°, 0°, and 20°, where a minus sign shows the trailing edge up. The wind tunnel model was mounted on a belly sting support located on the lower side of the model; the model and the support system are shown in Figure 2 (a). Previous results have shown an offset in the experimental pitch moment due to the wake formed behind the belly mounted sting.[15] Thus, for validation purposes the sting geometry has been added to CFD models.

In the wind tunnel experiments of DLR-F19, trailing-edge flap surfaces were removed from the wing and replaced by new surfaces for each combination of control surface deflections. For cases that inner and outer flaps are deflected at the same angle, the gaps between flaps were sealed. Figure 2 (b), for example, shows starboard flaps deflected 20 degrees and the sealed gaps between them. To validate CFD models for all these test cases, a separate high quality grid needs to be generated around aircraft for each control surface deflection; the grids should have sealed gaps between flaps in cases that neighboring flaps have the same deflection angle. However, this approach is very labor intensive and time consuming for all combinations of control surface deflections. Besides, for the response calculation of these flaps, a method is required to move surface(s) at each time of simulation without regenerating the grid. For these reasons, an overset grid approach is used in this work.

In more details, overlapping grids were generated individually for the wing and control surfaces, without the need to force grid points aligned with neighboring components. The control surface grids were then overset to the wing grid. However, a grid assembly approach typically requires some gaps between control surfaces and the wing which are not present in the wind tunnel tests. Besides, grid needs to be refined around the gaps which makes the grid size often larger than a single grid. In this work, a hybrid-grid RANS meshes was generated from the full geometry models of the DLR-F19 without control surfaces. The grids for inner and outer flaps were generated separately and overset onto the main grids. The gap between wing and control surfaces was set to 2mm.

The background and minor grids were generated in two steps. In the first step, the inviscid tetrahedral mesh was generated using the ICEMCFD code. This mesh was then used as a starting mesh by TRITET[44,45] which builds prism layers using an advancing front technique. TRITET rebuilds the inviscid mesh while respecting the size of the original inviscid mesh from ICEMCFD. The assembled grid of the full geometry is shown in Figure 3 which has a background mesh with around 129 million cells, and each minor grid with from

5.8 to 5.9 million cells. Figure 3(b) also shows the grid around starboard flaps, both deflected 20 degrees. The gaps between the wing and surfaces can be seen in this figure.

The gap regions between wing and control surfaces can become an issue with an overset grid approach because the large gaps could exhibit strong flow unsteadiness and affect the predictions. To study these effects, two single grids were generated for zero and maximum-minimum control surface deflections. These grids were also generated using ICEMCFD and TRITET codes and have the sting geometry. The grid with non-deflected surfaces is shown in Figure 4 (a) which has around 71 million cells. Note that the overset and single grids have very high resolutions. A third grid was therefore generated that has less resolution than other grids and has not the belly-mounted sting (it has around 40 million cells for full geometry). This mesh is shown in Figure 4 (b) and is used in this work to check the resolution and sting effects on the reduced order model predictions. This grid was generated using commercial grid generation code of Pointwise V17.01.R3 and exported in double precision format for use in Cobalt.

IV. Wind Tunnel Experiments

The DLR-F19 wind tunnel data are available from the low-speed wind tunnel facility in Braunschweig (DNW-NWB), Germany, which is an atmospheric wind tunnel of closed-circuit type and has a test section size of 2.8×3.25 m^2 with a maximum free stream velocity of 90 m/s.[12] The tunnel is capable of conducting static and dynamic measurements using different support systems; it can measure static forces and moments up to high angles of attack using a rear sting support in the $\alpha - \beta$ sweep configuration and can perform dynamic motions using the Model Positioning Mechanism (MPM) with a belly mounted support as shown in Figure 1 (a). Other available support systems are half-model setup, two-dimensional testing setup, and rotary motion support.

The DLR-F19 wind tunnel models were made with different combination of trailing edge control surfaces, such that all the gaps between surfaces are sealed. Static measurements were reported from MPM supports for angles of attack up to 30^o at different side-slip angle and control surface deflections. Mach number and Reynolds number in these tests were 0.146 and 1.58×10^6 based on a model reference length of 0.479 meter. Forces and moments were measured with an internal six component strain gauge balance.[12] The surface pressure distribution was measured by pressure tap rows at locations shown in Figure 5. Different connection links between the belly sting support and the internal balance at NWB provide an angle of attack range from 0 to 30 degrees. This is provided by two different rigid cranked yaw links or by using an internal pitch link driven by a seventh axis.

V. Results and Discussions

All simulations were run on the Cray XE6 machine at the Engineering Research Development Center (ERDC). The free-stream velocity in all simulations was fixed at Mach 0.146 and the Reynolds number is 1.58×10^6 similar to wind tunnel conditions. In steady simulations, first order accuracy in time with a CFL number of 1×10^6, and one Newton sub-iteration was used. In unsteady simulations, second-order accuracy in time and two Newton sub-iterations was used. For response function calculations and dynamic motions, however, five Newton sub-iterations was used. CFD Time steps of unsteady simulations were selected based on the non-dimensional time-step (Δt^*) criteria given in the work of Cummings *et al.*[46]

A. Validation

First validation results are presented for a configuration with no control surface deflections. This case corresponds to RN1001 test in the experiments. The CFD predicted results with several different turbulence models and using the overset grid approach are compared with experimental data of this test case in Figure 6. Figure 6 shows that the CFD predictions closely follow the trends of the experimental data up to moderate angles of attack. At higher angles, SRAC model slightly underestimates the experimental drag data. Both of the DDES models and the SST model perform better at the tested angle of attack of 10 degrees. Based on modeling assumptions, DDES models are more likely to predict vortex breakdown and separated flows at these angles. However, DDES simulations should run unsteady and typically require more iterations than classical turbulence models.

All tested turbulence models yield similar lift predictions at low angles of attack, but they result in

a spread of predictions at moderate to high angles. The low angles of attack offset between CFD and experimental pitch moment data is likely due to the effects of the belly sting mounting present in the experiments. Figure 6 shows that the SARC model is the worst performer of the models tested to predict the pitch moment, but it still provides results similar to the best performing SACCON simulations of the AVT-161 Task Group. Again the DDES models and the SST model perform better at ten degrees angle of attack. In more details, the SARC model does not capture the pitch break in the region of 16 to 17 degrees angle of attack particularly well. The drop in pitching moment from 16 to 16.5 degrees is small compared to the experimental data, and the flow appears to have moved to a different 'mode' by 17 degrees in the computational case, whereas it takes the experimental data until approximately 19 degrees to obtain the same pitching moment coefficient.

The experimental surface pressure distributions are available from spanwise taps at different chord length. The coordinates of these taps were input to the Cobalt. The code then writes the calculated flow parameters (selected by the user) at these locations. The files can be written at each iteration or report the time-averaged values from selected iterations. In this work, the pressure coefficients from the final iteration are used. These results are compared with measurements at different angles of attack and shown in Figure. 7. Each figure shows four set of lines at each experimental location.

Figure. 7 (a) shows that at zero degrees angle of attack, the difference in pressure between the upper and lower surfaces of the wing are small. The maximum difference occurs at 89% tap location close to the wing leading-edge due to tip vortices. At ten degrees angle of attack, the difference in pressures becomes large as shown in Figure. 7 (b). The tip vortices become stronger as well and their effects can be seen even at the tap location of 20%. An apex vortex is formed at 14^o which drops the upper surface pressure and therefore a dip is seen in the pressure plots of Figure. 7 (c) at tap locations of 20% and 45%. At 14^o angle of attack, the tip vortices are very strong; C_p values at these regions reach around -6. However, due to adverse pressure gradients, the tip vortices lose their strengths downstream around the tap location of 89%. At 16^o angle of attack, the apex vortices become stronger; therefore the dip in pressure plots become bigger and they stretch further downstream around the tap location of 67%. On the other hand, the tip vortices lose their strengths at this tap location. Above 16^o angle of attack, vortices start to interact, such that at 18^o angle of attack only one vortex is formed over the upper surface. At higher angles, this vortex breakdown and causes a high pressure region over the upper surface.

The vortex flow topology of the DLR-F19 is also shown in Figure 7. Two vortices emanating from the wing tip and apex are present at 14^o angle of attack (Fig. 7(c)). These vortices lead to a negative pressure region on the upper wing surface and hence augment the lift force. Figure 7 shows that at almost all locations, Cobalt predictions match well with experiments for angles of attack up to 16 degrees. As the angle of attack increases from 16^o, the onset point of the outboard vortex starts to travel toward the wing apex due to increasing adverse pressure gradients. The SARC results, however, start to underestimate the strength of these vortices for angles above 16^o, and by 17 degrees, the computational result is well underestimating the vortex strength at the 45 and 67% tap locations. This continues at 18 degrees, and to a much lesser extent at 20 degrees. At 18 degrees and above, the vortices are already interacting and there is a single vortex originating at the nose. It would appear that, despite using a steady temporal scheme, the SARC model manages to capture the dominant effect of that single vortex on the surface pressure, and resultant pitching moment coefficients. At higher angles of attack the tip vortex also breaks down. The interaction of the vortices produces a strong recirculation zone over the upper wing and results in wing stall and the aerodynamic center backward movement.

The next results are presented for RN1103 test case, in which, starboard flaps are deflected 20^o and port side flaps are deflected -20^o. The experiments were run over a sweep angle of attack range of 0^o to 30^o at zero side slip angle. Figure 8 shows all aerodynamic force and moment coefficients predicted from Cobalt using SARC turbulence model and measured in the experiments. The results show that RN1103 case does not show significant changes in the lift and drag forces from the baseline values because of the asymmetric flap deflections. However, the pitch moment slope falls in RN1103 case and its value at zero degrees angle of attack increases. CFD predictions also show an increase in the zero angle of attack pitch moment but the slope does not change as much as seen in experiments. Therefore, the comparison between CFD and experimental data looks better than was found for the cases with undeflected control surfaces. CFD data still underestimate lift coefficients at and above 20 degrees angle of attack. The flap deflections result in a negative roll moment that causes the right wing tip up and the left wing tip down. Figure 8 shows that the effect of the control surface deflections on rolling moment coefficient is underestimated at angles of attack

of 15 degrees and less, although it is well matched at 20 and 25 degrees. The pressure plots of RN1103 are also shown in Figure 9.

The overset grid results are compared with two single grids generated for RN1001 and RN1103 test cases. These comparisons allows us investigating the effects of the control surface gaps that exist for the overset grid on predictions. The single grids maintained, as much as possible, similar mesh distribution on the surface and the same density around the aircraft and control surfaces. Therefore, notwithstanding the effects of the hole-cut algorithm for the overset grid, it is likely that any differences between the two results are attributable to the existence of the gap. Figure shows the difference between the lift and pitching moment coefficients for the full-span overset grid compared with the half-span single grid for the case where the control surfaces are undeflected (RN1001). The pitch moment coefficient at an angle of attack of 10 degrees is 8% lower for the single grid than for the overset grid when using the SARC turbulence model, and similar differences arise for the SST model. The pitching moment coefficient for the single grid at the other two points sampled—angles of attack of 0 and 15 degrees—is also lower than the overset grid, but to a lesser extent. The exact reason for these differences is not immediately obvious. Figure 24b shows the difference between the rolling moment coefficients for the overset grid compared with the single grid for the case where the port control surfaces are deflected -20 degrees and the starboard control surfaces are deflected at +20 degrees (RN1103).

B. Modeling

The indical pitch moment responses of the DLR-F19 aircraft with a unit step change in angle of attack and pitch rate are shown in Fig. 11. None of control surfaces are deflected in these simulations. All calculations start from a steady-state solution at Mach number 0.146 and zero degrees angle of attack. For angle of attack response, the angle of attack is zero degrees at $t = 0$ and is held constant to one degree for all other times. The grid undergoes a translation motion but does not rotate. In pitch rate simulations, the grid starts to pitch up with a normalized pitch rate of $q = 1$ rad at $t = 0$ and the angle of attack is held to zero degrees during simulations with the aid of grid translation.

As shown in Figures 11(a)-(b), the z-axis force pitch moment responses have a negative peak at $t = 0$ followed by an increasing trend. As the steady flow around the vehicle is disturbed by the grid motion, a compression wave and an expansion wave are formed on the lower and upper surface of the vehicle that cause a sharp negative pitch moment peak in the responses.[27] As the response time progresses, the waves begin to move away from the vehicle and the force and pitch moment responses start to increase and then asymptotically reach the steady-state values. Note that final response values correspond to the steady-state solution at one degree angle of attack.

Figures 11(c)-(d) show initial jumps in the pitch rate responses as well. Likewise angle of attack response, the solutions will reach a steady-state value after a transient solution. Note that the final response values are dynamic derivatives of C_{Zq} and C_{mq} used in flight mechanic textbooks. A linear ROM was created using Eq. (5) and used for prediction of two small amplitude pitching motions. The motions are defines as $\alpha = \sin(\omega t)$ with frequencies of 1 and 2 Hz. The model predictions are compared with time-accurate simulations in Figure 12. The figure shows that linear ROM match CFD data very well. However, this model is only valid for linear regime of angle of attack. The functions of $C_{Z\alpha}$ and $C_{m\alpha}$ vary with angle of attack and thus a linear ROM cannot predict these effects.

To create a nonlinear model, angle of attack responses were simulated at different angles of attack and shown in Figure 13. In these simulations, the solution starts from a steady-state condition at angle of attack of α_k and then performing a unit step in the angle of attack for all $t > 0$. The response functions are then computed by taking the differences between time-varying forces and moments occurring after the step and the steady-state solution at $\alpha = \alpha_k$ degrees, and dividing them by the magnitude of the step ($\Delta\alpha$). For a weakly nonlinear system, the response will be nearly independent of the step magnitude (assuming that $\alpha_k + \Delta\alpha \leq \alpha_{k+1}$). Figure 13 shows that the responses at initial time are invariant with angle of attack, but the intermediate and final values change slightly with the angle of attack for the range of input considered. A nonlinear ROM was created and then using a linear interpolation scheme, the prediction of several pitching motion was evaluated. Figure 14 shows the results of two pitching motions defined as $\alpha = 5^o + 5^o\sin(\omega t)$ with frequencies of 1 and 2 Hz. Figure 14 shows that the nonlinear ROM predictions agree with CFD data much better than the linear model, but some discrepancies can be seen for angles above 6^o.

For pitching motions of $\alpha = 10^o + 4.7^o\sin(\omega t)$ with frequencies of 1 and 2 Hz, model predictions are compared with CFD and experimental data in Figure 15. The comparison shows that CFD data do not

match the experimental data. For more discussion of the DLR-F19 CFD and experimental dynamic cases, the reader is referred to the work of Young et al.[17] Model predictions follow the trends of CFD data not experimental, but they again show some discrepancies at high angles of attack. In all these models, it was assumed that angle of attack response change with angle of attack but not the pitch rate responses. Therefore, first test to check the source of discrepancy was to generate a new model that has pitch rate dependency on the angle of attack. The new model predictions are shown in Figure 15 (b) for the pitch moment. The results show that new model has very slight changes in the loop and data. Figure 16 compares the model and CFD data for a plunge motion as well. Grid undergoes only translation motions and and there is no rotation, therefore the pitch rate effects are zero. Even for this case, discrepancies can be seen between model and CFD data. These results clearly show that pitch-rate effects are not the source of discrepancy seen between model and CFD.

The response functions were calculated for the mesh without sting. These responses are different from those shown in Figure 13 because of mesh resolution and geometry differences. A new nonlinear model was created from these responses and used to predict pitching motions of $\alpha = 10^o + 4.7^o \sin(\omega t)$ with frequencies of 1 and 2 Hz. The model and CFD data are shown in Figure 17. Even for this mesh, discrepancies can be seen between the model and CFD data at high angles of attack. This confirms that the sting geometry is not the source of discrepancy seen between model and CFD as well.

VI. Conclusions

This paper investigates the use of ROMs that significantly reduce the CFD simulation time required to create a full aerodynamics database, and improve the accuracy of prediction of aircraft static and dynamic characteristics over quasi-steady predictions. The ROM considered was based on linear and nonlinear indicial response methods. The response functions consist of aircraft responses to step changes in the angle of attack, pitch rate, and control surface deflections. All these functions were calculated using direct response simulation in URANS with the aid of rigid grid motion tool. A time-dependent surrogate model was described to find the response functions dependency on the angles of attack and Mach numbers.

The test case used was the DLR-F19 which has complex vortex flow topology over the upper surface. The comparison between time-accurate simulations with ROM predictions showed the consistency of predictions for small angles of attack. The pitch moment models, however, do not match with CFD for higher angles of attack. The results showed that the sting geometry is not the source of discrepancies between CFD data and model predictions.

VII. Acknowledgements

Mehdi Ghoreyshi is supported by USAFA under contract FA70001320018; their financial support is gratefully acknowledged. Acknowledgements are expressed to the Department of Defense High Performance Computing Modernization Program (HPCMP), ERDC for providing computer time. The authors appreciate the support provided by the High Performance Computing Research Center at USAFA.

References

[1]Cummings, R. M. and Schütte, A., "The NATO STO Task Group AVT-201 on Extended Assessment of Stability and Control Prediction Methods for NATO Air Vehicles," 32nd AIAA Applied Aerodynamics Conference, AIAA, Reston VA (submitted for publication).

[2]Cummings, R. M. and Schütte, A., "An Integrated Computational/Experimental Approach to UCAV Stability & Control Estimation: Overview of NATO RTO AVT-161," AIAA Paper 2010–4392, June-July 2010.

[3]Schütte, A., Hummel, D., and Hitzel, S. M., "Numerical and Experimental Analyses of the Vortical Flow Around the SACCON Configuration," AIAA Paper 2010–4690, June-July 2010.

[4]Loeser, T. D., Vicroy, D. D., and Schütte, A., "SACCON Static Wind Tunnel Tests at DNW-NWB and 14′x22′ NASA LaRC," AIAA Paper 2010–4393, June-July 2010.

[5]Vicroy, D. D., Loeser, T. D., and Schütte, A., "SACCON Dynamic Wind Tunnel Tests at DNW-NWB and 14′x22′ NASA LaRC," AIAA Paper 2010–4394, June-July 2010.

[6]Cummings, R. M., Jirasek, A., Petterson, K., and Schmidt, S., "SACCON Static and Dynamic Motion Flow Physics Simulation Using Cobalt," AIAA Paper 2010–4691, June-July 2010.

[7]Frank, N., "Strategy for Dynamic CFD Simulations on SACCON Configuration," AIAA Paper 2010–4559, June-July 2010.

[8]Vallespin, D., Da Ronch, A., Badcock, K. J., and Boelens, O., "Validation of Vortical Flow Predictions for a UCAV Wind Tunnel Model," AIAA Paper 2010–4560, June-July 2010.

[9]Cummings, R. M. and Schütte, A., "Integrated Computational/Experimental Approach to Unmanned Combat Air Vehicle Stability and Control Estimation," *Journal of Aircraft*, Vol. 49, No. 6, 2012, pp. 1542–1557.

[10]Loeser, T. D., Vicroy, D. D., and Schütte, A., "Static and Forced-Oscillation Tests of a Generic Unmanned Combat Air Vehicle," *Journal of Aircraft*, Vol. 49, No. 6, 2012, pp. 1558–1583.

[11]Schütte, A., Hummel, D., and Hitzel, S. M., "Flow Physics Analyses of a Generic Unmanned Combat Aerial Vehicle Configuration," *Journal of Aircraft*, Vol. 49, No. 6, 2012, pp. 1638–1651.

[12]Loeser, T. and Bergmann, A., "Development of the Dynamic Wind Tunnel Testing Capabilities at DNW-NWB," AIAA Paper 2003-453, January 2003.

[13]Vallespin, D., Badcock, K. J., Da Ronch, A., White, M. D., Perfect, P., and Ghoreyshi, M., "Computational Fluid Dynamics Framework For Aerodynamic Model Assessment," *Progress in Aerospace Sciences*, Vol. 52, 2012, pp. 2–18.

[14]Ghoreyshi, M. and Cummings, R. M., "Unsteady Aerodynamics Modeling for Aircraft Maneuvers: a New Approach Using Time-Dependent Surrogate Modeling," AIAA Paper 2012-3327, June 2012.

[15]Jirasek, A. and Cummings, R. M., "Assessment of Sting Effect on X-31 Aircraft Model Using CFD," AIAA Paper 2010-1040, January 2010.

[16]Ghoreyshi, M. and Cummings, R. M., "Unsteady Aerodynamic Modeling of Aircraft Control Surfaces by Indicial Response Methods," *AIAA Journal*, in press.

[17]Young, M. E., Ghoreyshi, M., Jirasek, A., and Cummings, R. M., "Prediction and Validation of Aerodynamic Characteristics for a Generic UCAV Configuration with Trailing-Edge Flaps," 32nd AIAA Applied Aerodynamics Conference, AIAA, Reston VA (submitted for publication).

[18]Lofthouse, A. J., Ghoreyshi, M., Jirasek, A., and Cummings, R. M., "Static and Dynamic Simulations of a Generic UCAV Geometry Using the Kestrel Flow Solver," 32nd AIAA Applied Aerodynamics Conference, AIAA, Reston VA (submitted for publication).

[19]Schütte, A., Huber, K. C., and Boelens, O. J., "Static and Dynamic Numerical Simulations of a Generic UCAV Configuration With and Without Control Devices," 32nd AIAA Applied Aerodynamics Conference, AIAA, Reston VA (submitted for publication).

[20]Frink, N. T., "Dynamic Stability and Control CFD Investigations of a Generic 53-deg Swept UCAV Configuration," 32nd AIAA Applied Aerodynamics Conference, AIAA, Reston VA (submitted for publication).

[21]Lynch, E., Abras, J., Crowell, A. R., and Lee, J., "Static and Dynamic CFD Analysis of a Generic Swept Wing UCAV," 32nd AIAA Applied Aerodynamics Conference, AIAA, Reston VA (submitted for publication).

[22]Lisandrin, P., Carpentieri, G., and van Tooren, M., "Investigation over CFD-based Models for the Identification of Nonlinear Unsteady Aerodyanmics Responses," *AIAA Journal*, Vol. 44, No. 9, 2006, pp. 2043–2050.

[23]McDaniel, D. R., Cummings, R. M., Bergeron, K., Morton, S. A., and Dean, J. P., "Comparisons of CFD Solutions of Static and Maneuvering Fighter Aircraft with Flight Test Data," *Journal of Aerospace Engineering*, Vol. 223, No. 4, 2009, pp. 323–340.

[24]Tobak, M., "On the Use of the Indicial Function Concept in the Analysis of Unsteady Motions of Wings and Wing-Tail Combinations," NACA Report 1188, 1954.

[25]Leishman, J. G. and Nguyen, K. Q., "State-Space Representation of Unsteady Airfoil Behavior," *AIAA Journal*, Vol. 28, No. 5, 1989, pp. 836–844.

[26]Tobak, M. and Schiff, L. B., "On the Formulation of the Aerodynamic Characteristics in Aircraft Dynamics," NASA TR R–456, 1976.

[27]Ghoryeshi, M., Jirasek, A., and Cummings, R. M., "Computational Investigation into the Use of Response Functions for Aerodynamic Loads Modeling," *AIAA Journal*, Vol. 50, No. 6, 2012, pp. 1314–1327.

[28]Ghoreyshi, M. and Cummings, R. M., "Aerodynamics Modeling of a Maneuvering Aircraft Using Indicial Functions," AIAA Paper 2012–689, Jan 2012.

[29]Strang, W. Z., Tomaro, R. F., and Grismer, M. J., "The Defining Methods of Cobalt: A Parallel, Implicit, Unstructured Euler/Navier-Stokes Flow Solver," AIAA Paper 1999–0786, 1999.

[30]Gottlieb, J. J. and Groth, C. P. T., "Assessment of Riemann Solvers For Unsteady One-dimensional Inviscid Flows of Perfect Gasses," *Journal of Computational Physics*, Vol. 78, No. 2, 1988, pp. 437–458.

[31]Tomaro, R. F., Strang, W. Z., and Sankar, L. N., "An Implicit Algorithm For Solving Time Dependent Flows on Unstructured Grids," AIAA Paper 1997–0333, 1997.

[32]Tomaro, R. F., Strang, W. Z., and Wurtzler, K. E., "Can Legacy Codes Scale on Tens of Thousands of PEs or Do We Need to Reinvent the Wheel?" 2012 High Performance Computing Modernization Program Contributions to DoD Mission Success, pp. 231-236, September 2012.

[33]Spalart, P. R. and Allmaras, S. R., "A One Equation Turbulence Model for Aerodynamic Flows," AIAA Paper 1992–0439, January 1992.

[34]Swanson, R. C. and Rumsey, C. L., "Numerical Issues for Circulation Control Calculations," AIAA Paper 2008-3008, June 2008.

[35]Bigarella, E. and Azevedo, J., "Advanced Eddy-Viscosity and Reynolds-Stress Turbulence Model Simulations of Aerospace Applications," *AIAA Journal*, Vol. 45, No. 10, 2007, pp. 2369–2390.

[36]Churchfield, M. J. and Blaisdell, G. A., "Reynolds Stress Relaxation Turbulence Modeling Applied to a Wingtip Vortex Flow," *AIAA Journal*, Vol. 51, No. 11, 2013, pp. 2643–2655.

[37]Spalart, P. R. and Shur, M. L., "On the Sensitization of Turbulence Models to Rotation and Curvature," *Aerospace Science Technology*, Vol. 1, 1997, pp. 297302.

[38]Spalart, P. R., Jou, W.-H., Strelets, M., and Allmaras, S. R., "Comments on the Feasibility of LES for Wings, and on a Hybrid RANS/LES Approach," In Proceedings, 1st AFSOR International Conference on DNS/LES, Greyden Press, Columbus, OH, 1997, pp. 137147.

[39]Trapier, S., Deck, S., and Duveau, P., "Delayed Detached-Eddy Simulation and Analysis of Supersonic Inlet Buzz," *AIAA Journal*, Vol. 46, No. 1, 2008, pp. 118–131.

[40]Tuncer, I. H., Gulcat, U., Emerson, D. R., and Matsuno, K., *Parallel Computational Fluid Dynamics 2007*, Springer-Verlag,Germany, 2009.

[41]Roskam, J., "Airplane Design," 1990, Roskam Aviation and Engineering Corporation, Kansas, USA.

[42]Bisplinghoff, R. L. Ashley, H. and Halfman, R. L., *Aeroelasticity*, Dover Publications, Mineola, N.Y., 1996.

[43]Singh, R. and Baeder, J., "Direct Calculation of Three-Dimensional Indicial Lift Response Using Computational Fluid Dynamics," *Journal of Aircraft*, Vol. 34, No. 4, 1997, pp. 465–471.

[44]Tyssel, L., "Hybrid Grid Generation for Complex 3D Geometries," Proceedings of the 7th International Conference on Numerical Grid Generation in Computational Field Simulation, 2000, pp. 337–346.

[45]Tyssel, L., "The TRITET Grid Generation System," International Society of Grid Generation (ISGG)," Proceedings of the 10the International Conference on Numerical Grid Generation in Computational Field Simulations, 2000.

[46]Cummings, R. M., Morton, S. A., and McDaniel, D. R., "Experiences in Accurately Predicting Time-Dependent Flows," *Progress in Aerospace Sciences*, Vol. 44, 2008, pp. 241–257.

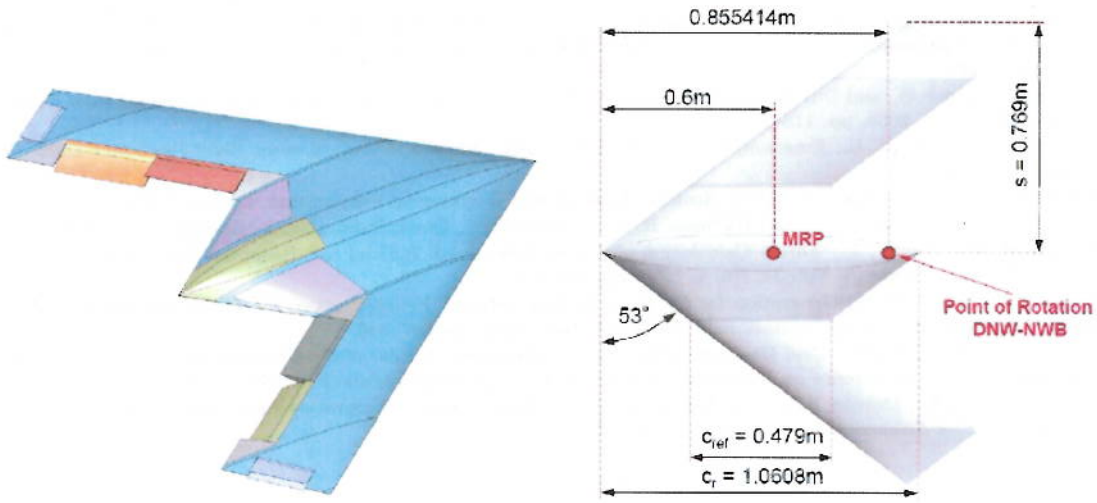

(a) DLR-F19 with control surfaces

(b) Geometry details

Figure 1. The DLR-F19 configuration.[19]

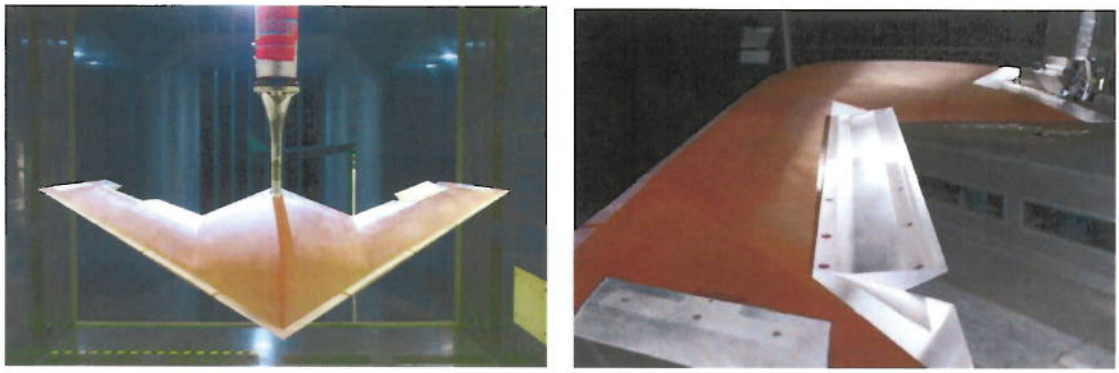

(a) Wind tunnel model on the MPM support

(b) Control surfaces

Figure 2. The DLR-F19 wind tunnel model and control surfaces.[19] In (b) starboard Control surfaces are shown with 20 degrees deflections.

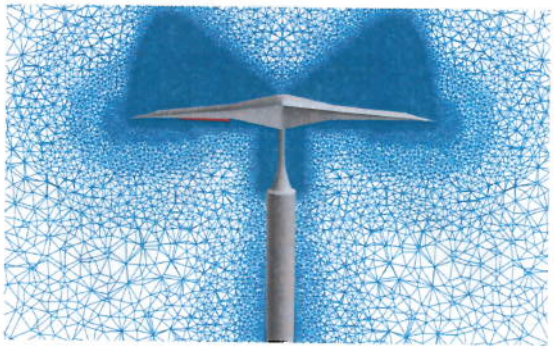

(a) Grid overview

(b) Surface grids

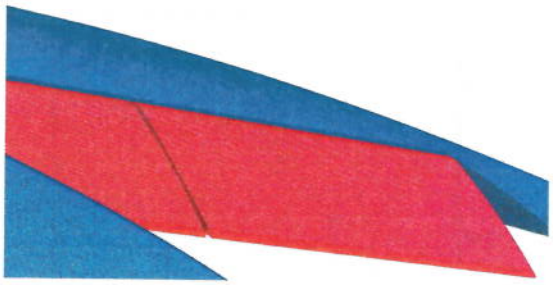

(c) Starboard flaps and gaps

Figure 3. The full-geometry overset grid. In this grid, starboard flaps are deflected 20^o and port flaps deflected -20^o.

(a) With sting

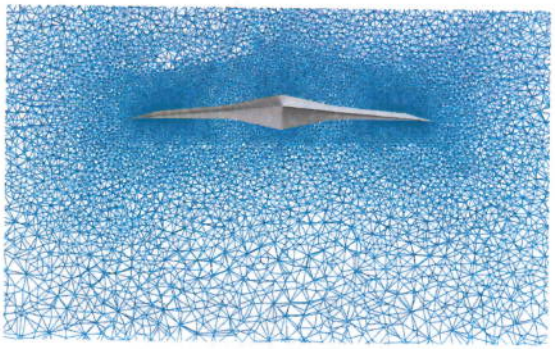

(b) Without sting

Figure 4. The DLR-F19 single grids. In both grids, all control surfaces have zero deflection angle.

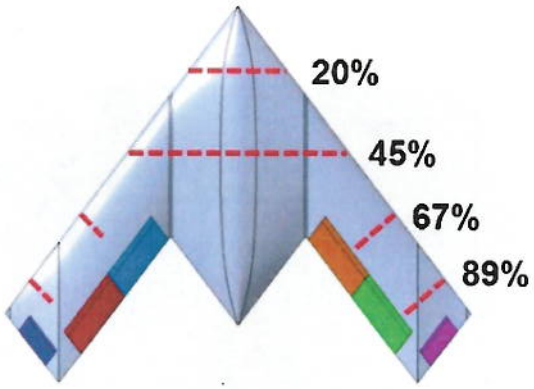

Figure 5. Pressure tap locations of the DLR-F19 wind tunnel model.[19]

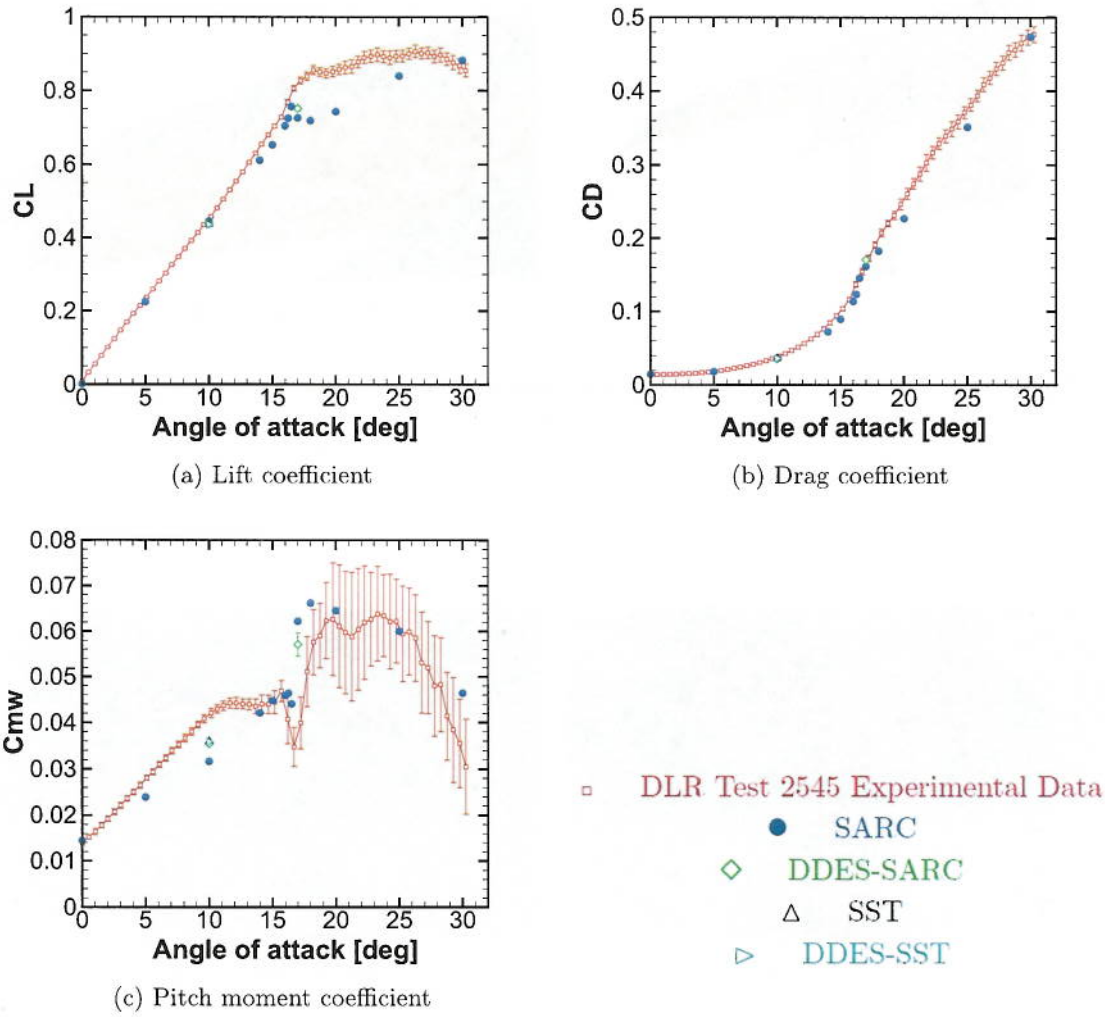

(a) Lift coefficient

(b) Drag coefficient

(c) Pitch moment coefficient

Figure 6. The RN1001-case coefficients. Control surfaces are not deflected. Test conditions correspond to M=0.146, Re=1.58×10^6 and β=0.

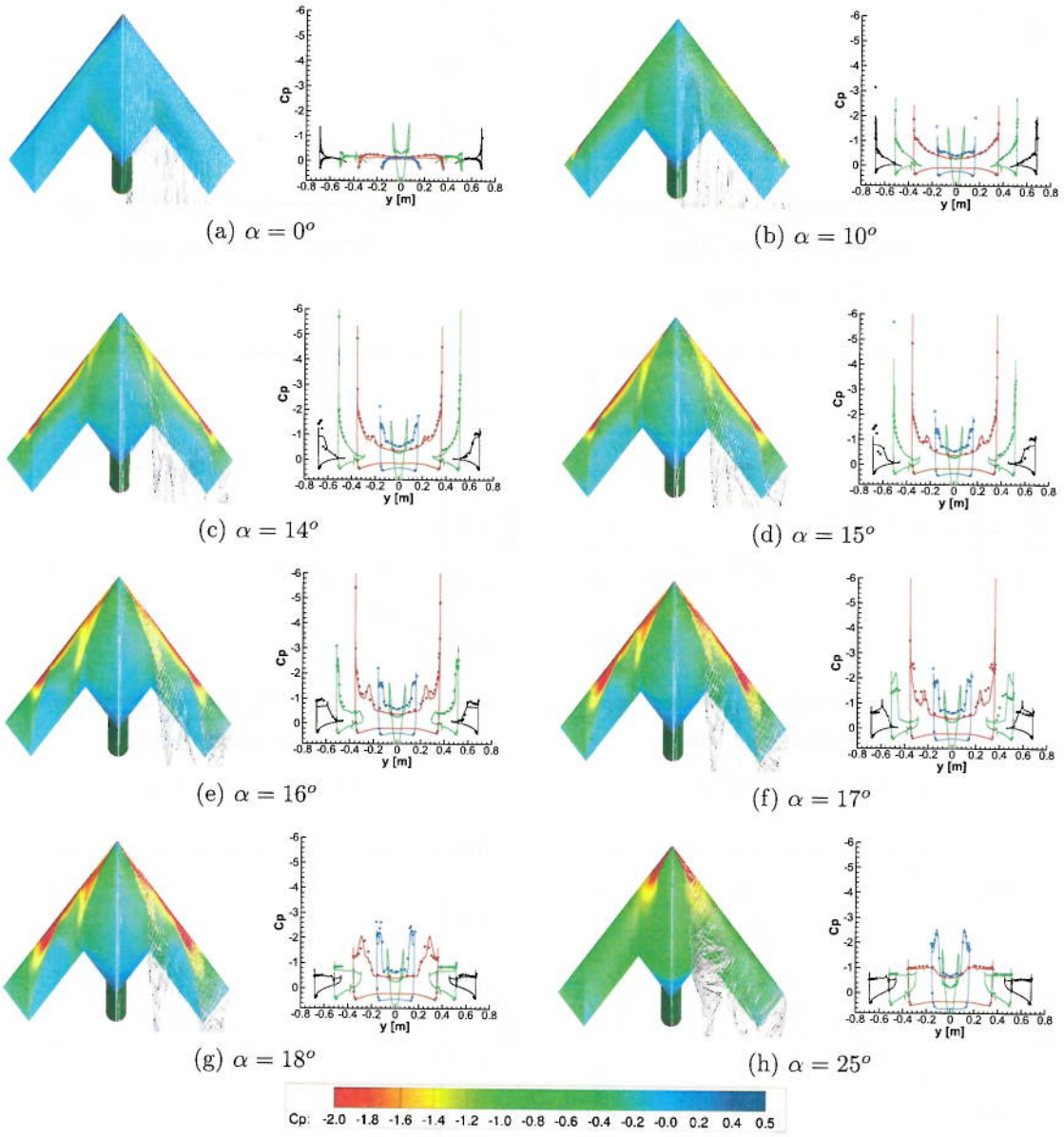

(a) $\alpha = 0^o$ (b) $\alpha = 10^o$

(c) $\alpha = 14^o$ (d) $\alpha = 15^o$

(e) $\alpha = 16^o$ (f) $\alpha = 17^o$

(g) $\alpha = 18^o$ (h) $\alpha = 25^o$

Figure 7. The RN1001-case surface pressures using SARC turbulence model. Control surfaces are not deflected. Test conditions correspond to M=0.146, Re=1.58×10^6 and β=0. In above pressure plots, lines show CFD predictions.

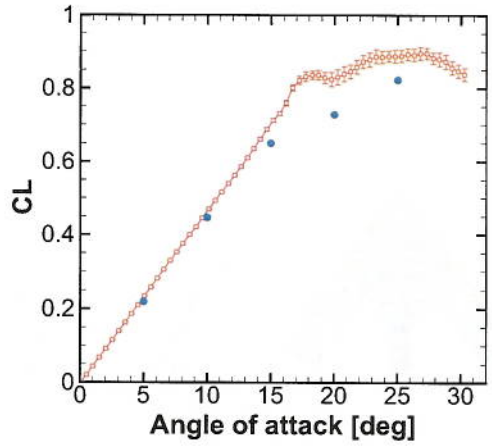

(a) Lift coefficient

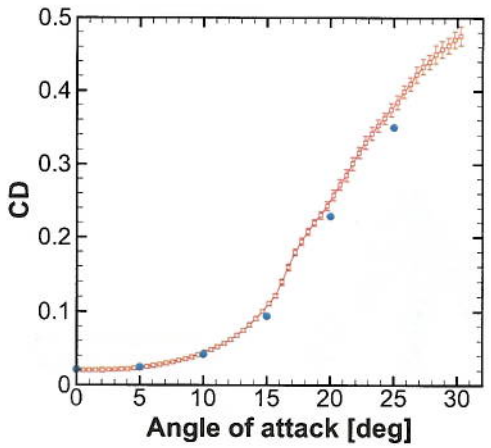

(b) Drag coefficient

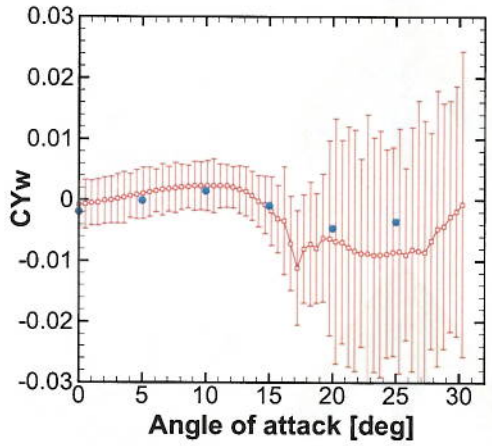

(c) Side-force coefficient

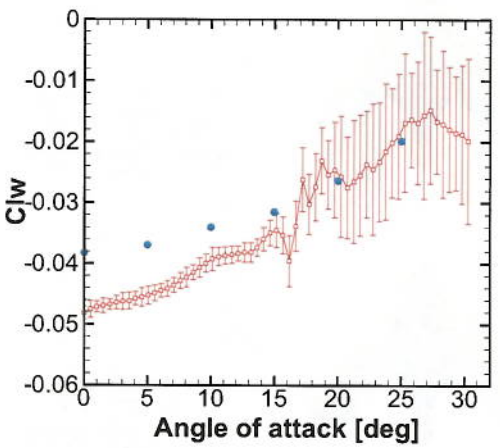

(d) Roll moment coefficient

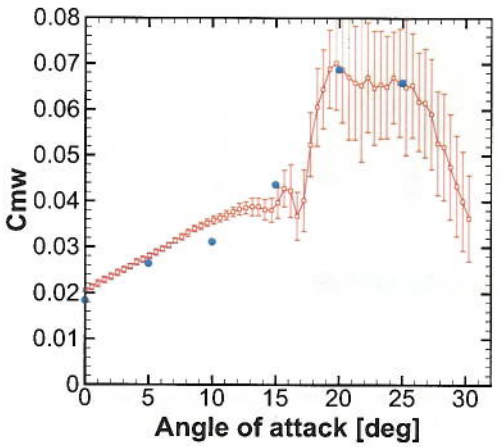

(e) Pitch moment coefficient

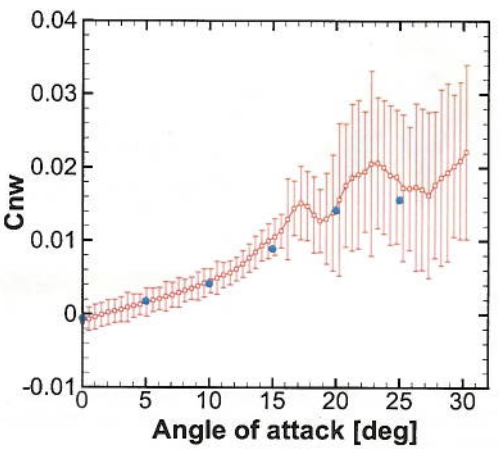

(f) Yaw moment coefficient

Figure 8. The RN1103-case coefficients. Control surfaces are fully deflected. Test conditions correspond to M=0.146, Re=1.58×10^6 and β=0. In all figures, prediction are from Cobalt using SARC turbulence model and shown with a blue-colored dot. Forces and moments are reported in the wind axes.

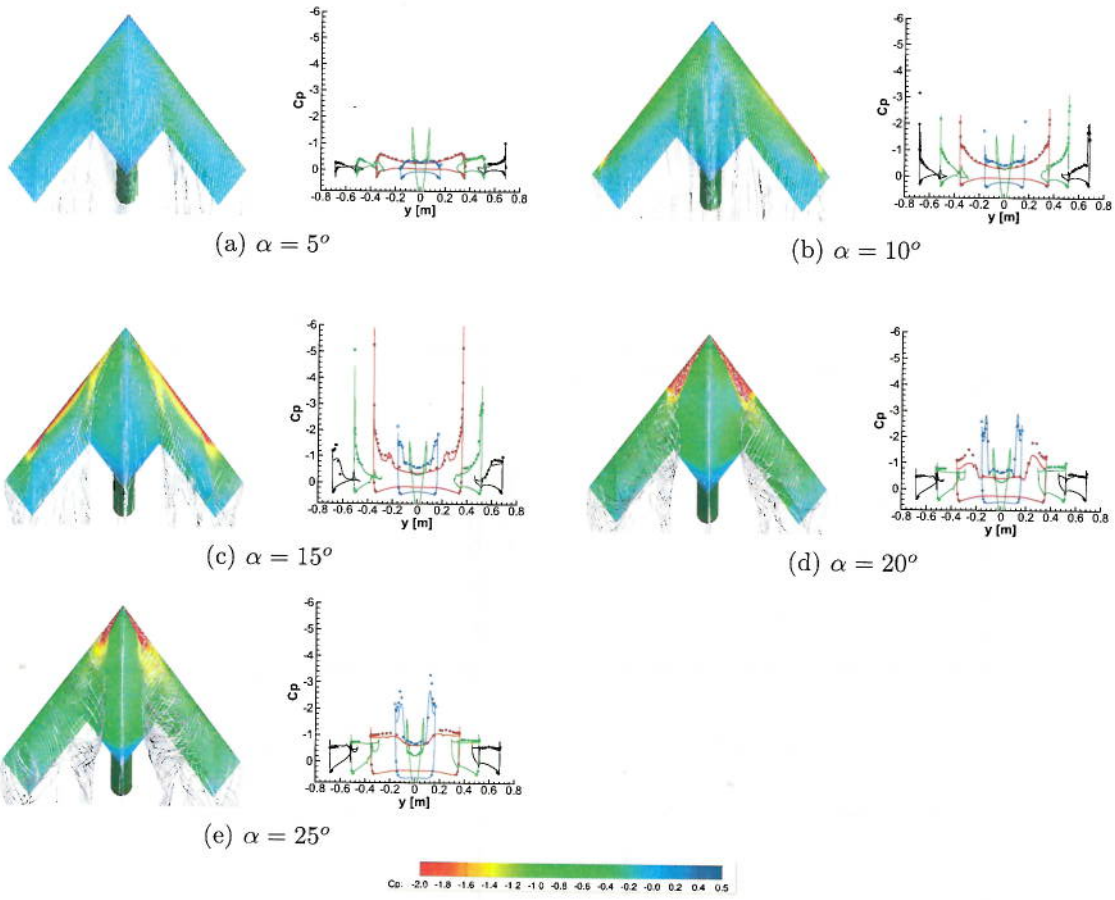

(a) $\alpha = 5^o$ (b) $\alpha = 10^o$

(c) $\alpha = 15^o$ (d) $\alpha = 20^o$

(e) $\alpha = 25^o$

Figure 9. The RN1103-case surface pressures using SARC turbulence model. Control surfaces are fully deflected. Test conditions correspond to M=0.146, Re=1.58×10^6 and β=0. In above pressure plots, lines show CFD predictions.

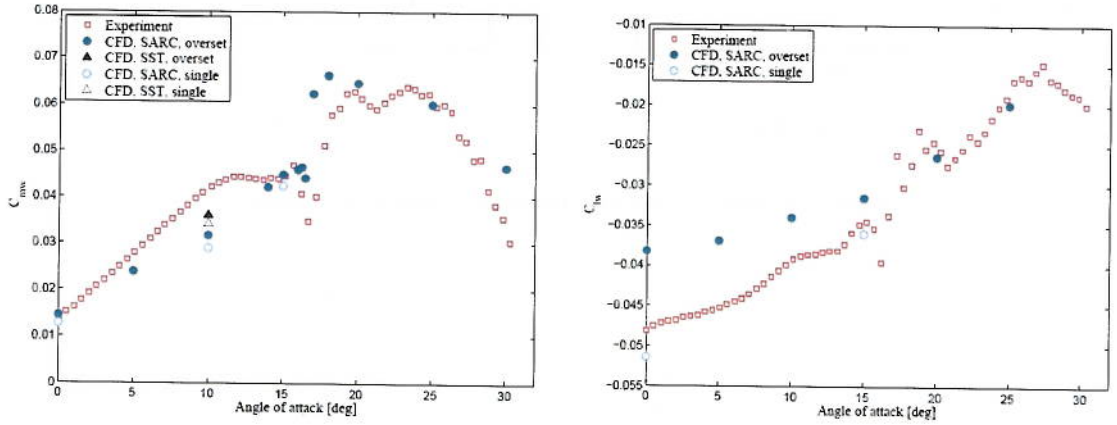

(a) RN1001- pitch moment coefficient (b) RN1103- Roll moment coefficient

Figure 10. Comparing overset grid results with results for a single grid.

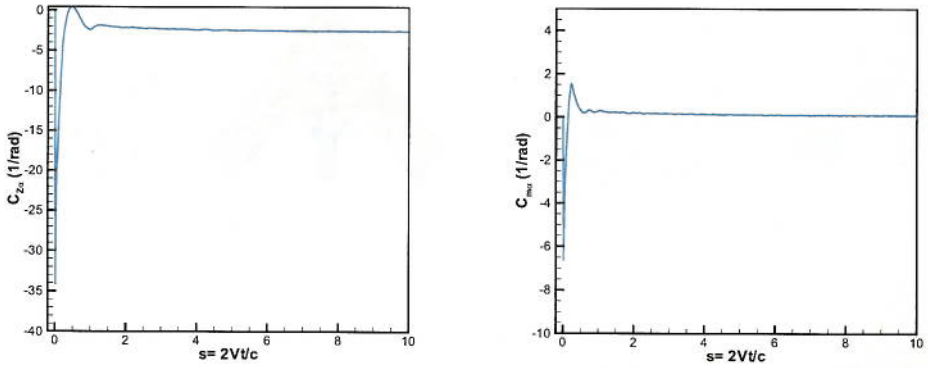

(a) $C_{Z\alpha}$ response

(b) $C_{m\alpha}$ response

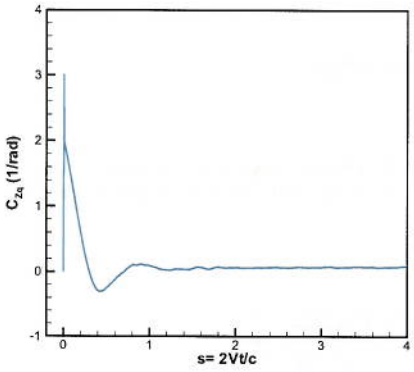

(c) C_{Zq} response

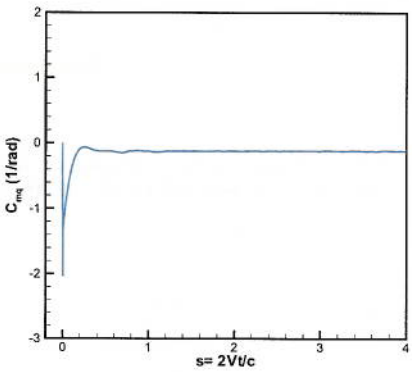

(d) C_{mq} response

Figure 11. Linear angle of attack and pitch rate responses.

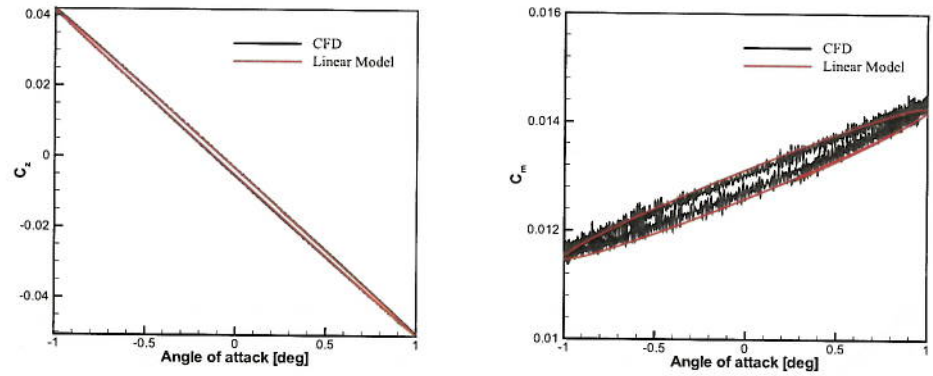

(a) f =1Hz

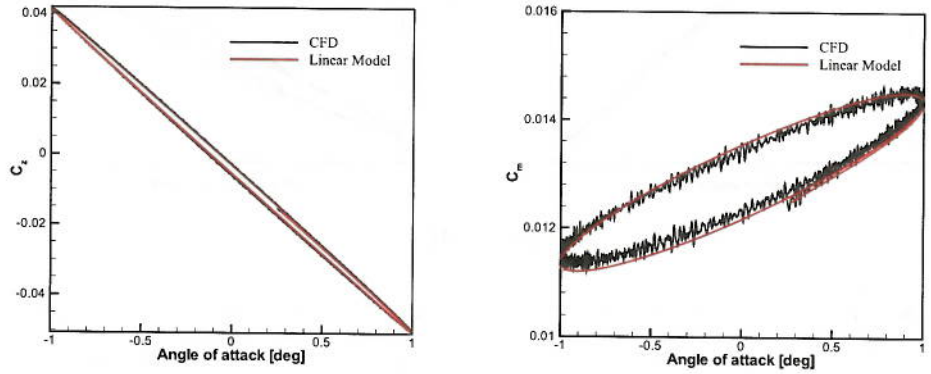

(b) f =2Hz

Figure 12. Linear ROM modeling for pitch motions defined as $\alpha = \sin(\omega t)$

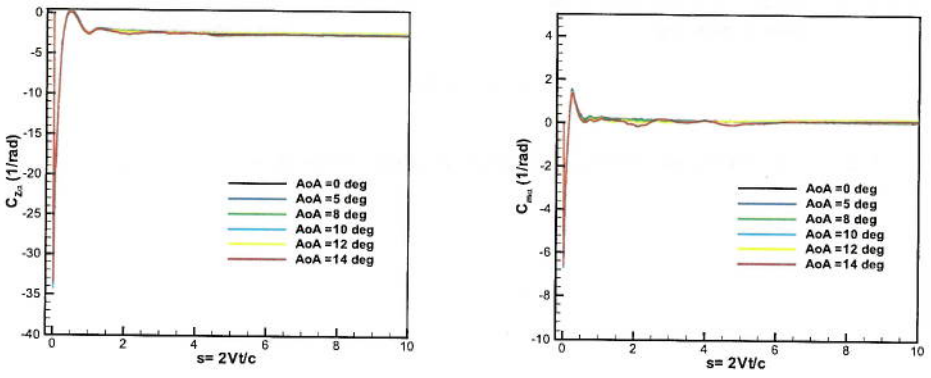

(a) $C_{Z\alpha}$ responses

(b) $C_{m\alpha}$ responses

Figure 13. Angle of attack nonlinear responses.

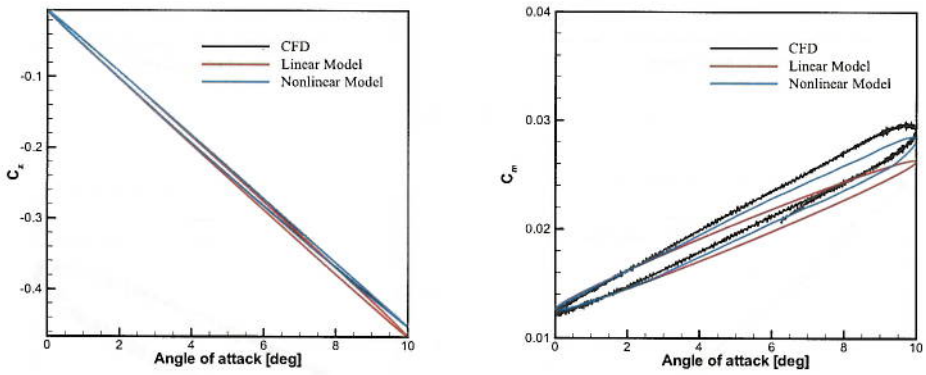

(a) f =1Hz

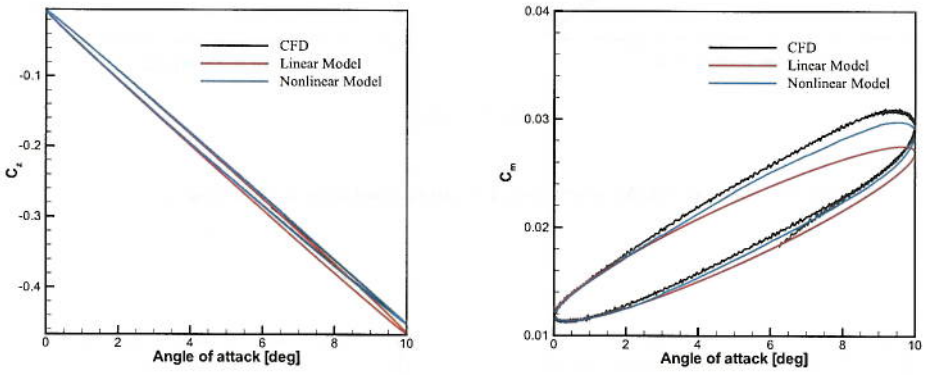

(b) f =2Hz

Figure 14. ROM predictions for pitch motions defined as $\alpha = 5 + 5\sin(\omega t)$

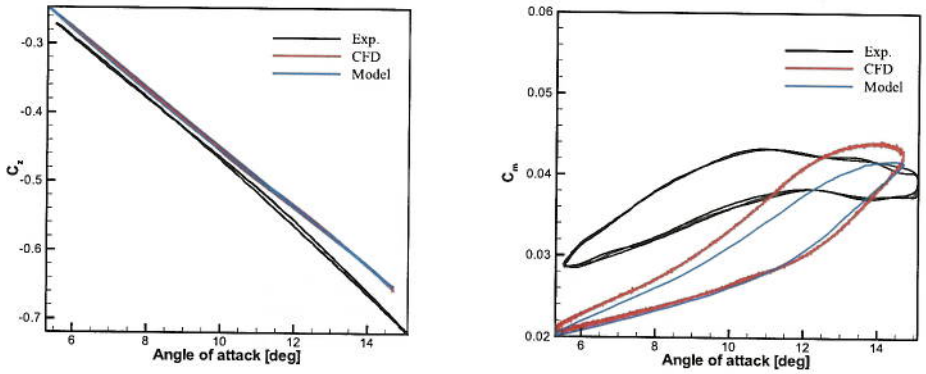

(a) f =1Hz

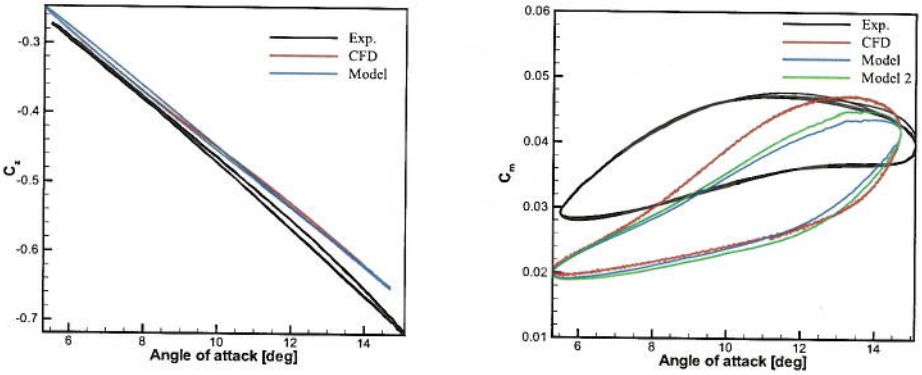

(b) f =2Hz

Figure 15. ROM predictions for pitch motions defined as $\alpha = 10 + 4.7\sin(\omega t)$. In model, pitch rate response was calculated at zero degrees angle of attack. In Model 2, pitch rate responses depend on the angle of attack.

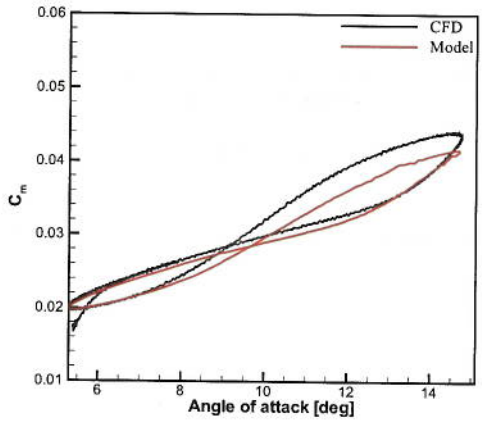

Figure 16. ROM predictions for a plunge motion defined as $\alpha = 10 + 4.7\sin(\omega t)$ with f = 2Hz.

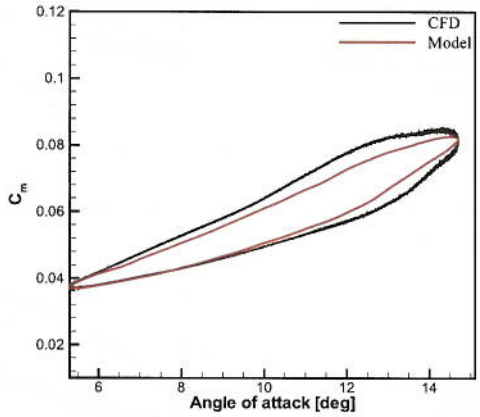

(a) f =1Hz

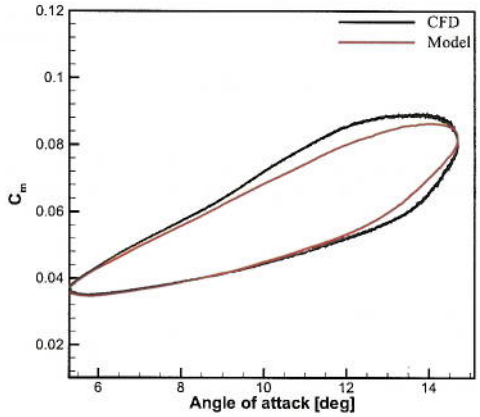

(a) f =2Hz

Figure 17. ROM predictions for pitch motions defined as $\alpha = 10 + 4.7\sin(\omega t)$. The mesh has no sting geometry.